

CHALMERS
UNIVERSITY OF TECHNOLOGY

Modeling and Implementation of Inductive Brushless Exciter for Superconducting Synchronous Machines

Downloaded from: https://research.chalmers.se, 2026-11-23 09:22 UTC

Citation for the original published paper (version of record):
Lai, L., Jang, H., Tang, J. et al (2026). Modeling and Implementation of Inductive Brushless Exciter for Superconducting Synchronous
Machines. 2022 IEEE International Conference on Environment and Electrical Engineering and 2022 IEEE Industrial and Commercial Power Systems Europe, EEEIC / I and CPS Europe 2022, In Press.
http://dx.doi.org/10.1109/TIA.2026.3728746

N.B. When citing this work, cite the original published paper.

© 2026 IEEE. Personal use of this material is permitted. Permission from IEEE must be obtained for all other uses, in any current or future media, including reprinting/republishing this material for advertising or promotional purposes, or reuse of any copyrighted component of this work in other works.

(article starts on next page)

2026-EMC-0254.R2

Modeling and Implementation of Inductive Brushless Exciter for Superconducting Synchronous Machines

Linhua Lai, Hyungkwan Jang, Junfei Tang, Byungho Min, Yujing Liu

***Abstract*—Superconducting (SC) machines are increasingly favored for high-power-density applications due to low losses in field windings while generating high magnetic flux. To transfer power to the field winding, brushless exciters are a promising solution as friction is eliminated. However, conventional brushless exciters in SC machines are bulky. A general approach to reduce size is to increase the frequency of power transfer. Nevertheless, the existing high-frequency exciters do not fit SC machines due to the extremely low-voltage and high-current of SC field windings. In this study, the feasibility of applying high-frequency brushless exciters to SC machines is investigated. Firstly, an analytical model is developed to characterize the excitor, including output current and losses. Then, finite-element simulations are performed to assist the design of rotating transformer to reduce AC resistance and branch imbalance. In the end, an exciter is prototyped and tested. The prototype successfully transfers the required amount of current to the load, which proves the feasibility of applying high-frequency brushless exciters to SC machines.**

***Index Terms*— Superconducting machines, Brushless excitation, Rotating transformer, High-temperature superconductors, Synchronous motors, Electrical excited synchronous machines.**

I. INTRODUCTION

COMPARED to conventional electric machines, superconducting (SC) machines offer several advantages, including lower energy losses, higher magnetic field capabilities, and significantly greater power density[1]. These benefits make SC machines particularly attractive for high-power-density applications such as electrically propelled aircraft [2], [3], marine vessels [4], and large-scale wind turbine generators [5]. The progress of high-temperature superconducting (HTS) wire technology has enabled the consideration of SC machines in increasingly compact and high-power-density systems, where constraints on size, efficiency, and reliability apply. With a more compact design of SC machines, space can be freed for energy storage systems or passenger accommodation, which offers significant benefits for applications such as electrically propelled aircraft and heavy-duty vehicles. However, due to the technological limitations in fabricating superconducting joints with sufficiently low resistance, a continuous excitation system—commonly referred to as a flux pump—is required to maintain the excitation current in SC coils [6]. Such excitation hardware can pose a challenge to system design, as it may reduce the compactness and power-density of system. These constraints and challenges are particularly critical for machines with SC rotor windings, where excitation systems must be integrated within the rotating structure.

Various types of excitation systems for superconducting coils have been proposed in previous studies. Broadly, these systems can be categorized into four types: DC dynamos, linear-motor type, pulse-type , and transformer-rectifier type [7]. The DC-dynamo excitation, which is illustrated in [7], [8], induces voltage in SC coils using rotating magnets, but requires an additional drive machine to provide mechanical motion, increasing system complexity and limiting compactness. Pulse-type excitation systems have mainly been demonstrated in non-rotating configurations [9], [10]. Although mechanically contactless, these systems rely on traveling magnetic fields generated through sequential pulsed excitation of stationary coils, which complicates their extension to SC rotor excitation. In [11], [12], a prototype linear-motor-type excitation system has been demonstrated for superconducting machines. However, external DC and AC power supplies are required to generate the travelling-wave current, leading to increased system size and auxiliary components, thereby limiting its applicability to compact SC rotor applications. Transformer-rectifier excitation systems are explored in [13], [14], [15], [16], [17]. In this configuration, AC current is transferred from the primary to the secondary winding of a transformer without mechanical contact. Switching elements on the secondary side then rectify the AC current into DC, which is supplied to the SC coils.

Among these excitation approaches, transformer-rectifier systems have been shown to offer higher achievable excitation current and simpler system integration, making them particularly attractive for superconducting machine applications [13], [16]. The transformer-rectifier excitation

Linhua Lai, Junfei Tang, Yujing Liu are with the Department of Electrical Engineering, Chalmers University of Technology, 41296 Gothenburg, Sweden (E-mail: linhua@chalmers.se; junfei.tang@chalmers.se; yujing.liu@chalmers.se).

Hyungkwan Jang is with the Drive & Magnetic Material Development Team, Hyungdai Motor Company Gyeonggi-do, Republic of Korea (E-mail: janghk@hyundai.com)

Byungho Min is with the Power System Material Development team Hyungdai Motor Company Gyeonggi-do, Republic of Korea (E-mail: mbh8994@hyundai.com)

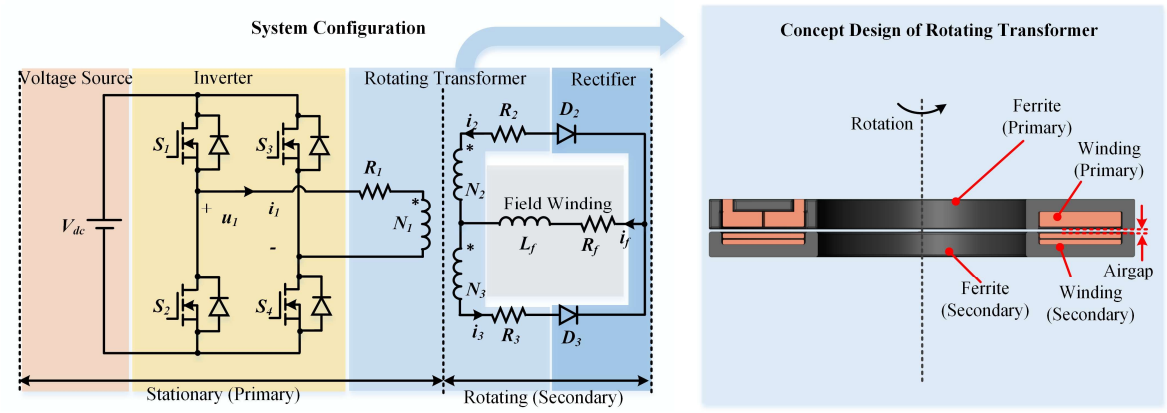

Fig. 1 System configuration of the proposed brushless exciter (a) Topology of the system. (b) Cross-sectional view of the pot-core rotating transformer (RT)

system is considered a promising solution for SC rotor applications due to several key advantages. First, it eliminates the need for brushes and slip rings, thereby avoiding mechanical friction between stationary and rotating parts. As a result, maintenance requirements—such as lubricating contact surfaces—are significantly reduced [18]. Second, this type of exciter can be powered by a DC voltage source, making it compatible with systems that use batteries or fuel cells [19]. Additionally, since no rotating components are required to drive the exciter, the overall mechanical design becomes simpler and more compact. However, the relatively large size and weight of transformer-rectifier exciters can be a drawback [20]. To address this, the size of the exciter can be reduced by increasing either the magnetic flux density or the operating frequency. Given that flux density is limited by the saturation of available core materials, brushless exciters operating at high frequencies have emerged as a more viable and effective solution [21].

High-frequency brushless excitation system (BES) have been employed in electrically excited synchronous machines (EESM) in previous studies [22], [23], [24]. The performance of EESM with high-frequency brushless exciter has been shown to be comparable to that of brush-based machines and permanent magnet synchronous machines (PMSM) [25], [26]. However, the research on high-frequency BES for SC machine remains insufficient. Existing studies mainly focus on conventional field windings and moderate current levels and therefore have not addressed the loss mechanisms and design constraints that arise under low-impedance, high-current operation required by SC field windings. Under such conditions, existing designs tend to generate high losses in the AC windings and rectifier components. To address these challenges, the exciter topology must be selected to enable reliable high-current operation. In particular, the transformer design should be configured to achieve low AC losses under high-frequency conditions. Furthermore, an accurate analytical model is required to characterize the relationships among field winding current, component parameters, and loss mechanisms, thereby providing a foundation for systematic design and analysis.

The objective of this paper is to investigate the feasibility of applying a high-frequency brushless exciter to SC machine application. First, an analytical model of the high-frequency brushless exciter is developed to evaluate the influence of transformer and rectifier parameters on the output excitation current. Then, the losses in each component of the brushless exciter are modeled and analyzed. Next, to reduce AC losses in the transformer, finite-element method (FEM) simulations are performed to examine the magnetic field distribution and AC resistance under different winding configurations. Finally, a prototype brushless exciter is constructed and tested on a SC motor to validate the analysis.

II. System Configuration and Modeling

A. System Configuration

To deliver the high current required by the SC motor, the topology of the excitation system is shown in Fig. 1 (a). The system transfers power from a DC voltage source to the SC field winding wirelessly through a rotating transformer. Hence the mechanical contact between stationary power source and the rotating machine is avoided. Such a system consists of a DC voltage source, an H-bridge inverter, a center-tap rotating transformer (RT), and a full-wave rectifier. The H-bridge inverter converts the DC voltage into a high-frequency AC square wave. This AC voltage is applied to the primary winding of the center-tap transformer, which is magnetically coupled to the secondary winding. To handle the high field winding current, the secondary side is split into two branches, each composed of stacked coils. During each switching cycle, the branches conduct alternately. The output current is delivered to the load through a full-wave rectifier, which offers a lower forward voltage drop compared to a conventional H-bridge rectifier, thereby reducing conduction losses in the diodes. Meanwhile, as each branch conducts for half a period, the use of diodes with lower current ratings is allowed.

During normal operation, the primary side of the transformer remains stationary, while the secondary side rotates at the same speed as the SC motor. A cross-sectional view of the transformer is shown in Fig. 1 (b). The transformer can be made as a pot-core design. Since there is no axial movement during rotation, the air gap remains constant, ensuring that the mutual inductance between windings is unaffected by the rotation [27].

As the system is intended to be compact, strong magnetic coupling between the stationary and rotating parts of the

transformer is assumed. Under this condition, the leakage inductance in the rotating transformer is small and the system allows sufficient current transfer and satisfying power factor without resonance. Therefore, the extra components required by resonant-based circuit can be saved. Hence, the number of components is reduced, and the complexity of the circuit is minimized.

B. Modeling of Brushless Exciter

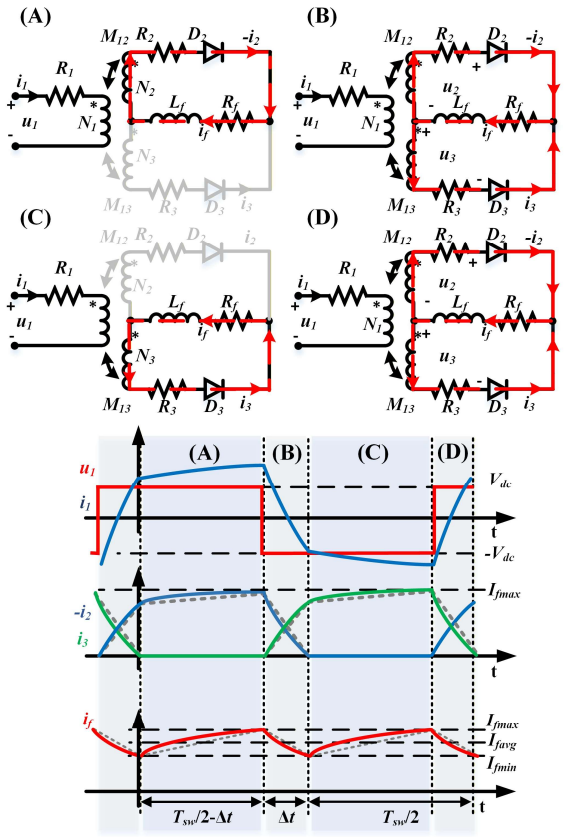

Fig. 2 Schematic of the operating modes of the brushless exciter

To obtain the gain of the proposed brushless exciter, the mathematical model should be built. Fig. 2 illustrates the operating modes and key waveforms of the brushless exciter. The input voltage u_1 is a square wave with fixed period T_{sw}, generated by the inverter. The current i_1 in the primary winding N_1 is coupled to the secondary windings N_2 and N_3, where the currents i_2 and i_3 are induced, respectively.

Determined by the magnitudes of i_2 and i_3, the operation of the brushless exciter consists of four phases A, B, C, and D. Assuming that the parameters of two branches are identical, phases A and B mirror phases C and D. Hence, only phases A and B are analyzed here.

In phase A, the field winding current i_f is fully supplied by the upper branch N_2 with current i_2. The field current transitions to the lower branch N_3 during commutation phase B, which lasts until the current i_2 is fully discharged. Denote the time of the commutation phase is Δt.

In phase A, the field winding is energized through winding N_2. The field winding current i_f is conducting through upper branch, thus

$$\begin{cases} i_2 = -i_f \\ i_3 = 0 \end{cases}. \tag{1}$$

The currents are governed by the properties of the transformer windings. The relationship between the current and voltage of RT can be described as

$$u_1 = L_1 \frac{di_1}{dt} + M_{12} \frac{di_2}{dt} + R_1 i_1 \tag{2}$$

$$u_2 = M_{21} \frac{di_1}{dt} + L_2 \frac{di_2}{dt} + R_2 i_2 \tag{3}$$

where L_1 and L_2 are the self inductance of windings N_1 and N_2, respectively. M_{12}=M_{21} are the mutual inductance between windings. R_1 and R_2 are the resistance of windings. u_2 is the terminal voltage of N_2.

Additionally, the terminal voltage u_1 and u_2 can be described as

$$u_1 = V_{dc} - i_1(2R_{MOSFET} + R_1) \tag{4}$$

$$u_2 = v_{fw} - i_2 R_{diode} + L_f \frac{di_f}{dt} + i_f R_f \tag{5}$$

where v_{fw} is the constant forward voltage drop of the diode, R_{diode} is the equivalent on resistance of the diode, and R_{MOSFET} is the on-state resistance of the MOSFET in the inverter.

Given that the forward voltage drops on the power MOSFETs and equivalent resistance of stationary winding are significantly smaller than the DC link voltage (i.e. (i_1R_{MOSFET}+ i_1R_1)<<V_{dc}), simplifications can be made to derive the expression for the field current during the charging phase. From (1)-(5), it can be deduced that when $t\in[0, T_{sw}/2-\Delta t)$, the field winding is charged, and the field current can be described as

$$(\frac{M_{12}^2}{L_1} - L_2 - L_f)\frac{di_f}{dt} - (R_2 + R_{diode} + R_f)i_f + \frac{M_{12}}{L_1}V_{dc} - v_{fw} = 0\,. \tag{6}$$

By solving (6), the field winding current is derived

$$i_f(t) = \frac{\frac{M_{12}}{L_1}V_{dc} - v_{fw}}{R_2 + R_{diode} + R_f} + C_1 e^{\frac{-(R_2+R_{diode}+R_f)}{L_f+L_2-M_{12}^2/L_1}t}\,. \tag{7}$$

When t=0, i_f=I_{fmin}, C_1 can be derived as

$$C_1 = \frac{(R_2 + R_{diode} + R_f)I_{fmin} + v_{fw} - \frac{M_{12}}{L_1}V_{dc}}{R_2 + R_{diode} + R_f}\,. \tag{8}$$

In phase B, both N_2 and N_3 conduct simultaneously, and the field current is the sum of the currents in both branches, that is

$$i_3 - i_2 = i_f\,. \tag{9}$$

The RT model is extended as

$$V_{dc} = L_1 \frac{di_1}{dt} + M_{12} \frac{di_2}{dt} + M_{13} \frac{di_3}{dt} \tag{10}$$

$$u_2 = M_{21} \frac{di_1}{dt} + L_2 \frac{di_2}{dt} + M_{23} \frac{di_3}{dt} + R_2 i_2 \tag{11}$$

$$u_3 = M_{31} \frac{di_1}{dt} + M_{32} \frac{di_2}{dt} + L_3 \frac{di_3}{dt} + R_3 i_3 \tag{12}$$

where u_3 is the terminal voltage of N_3. L_3 is the self inductance of N_3. R_3 is the resistance of N_3. M_{23}=M_{32} is the mutual inductance between N_2 and N_3. M_{13}=M_{31} is the mutual inductance between N_1 and N_3.

The terminal voltage u_2 follows (5). Meanwhile, the terminal voltage u_3 can be described using field winding current i_f as

$$u_3 = -v_{fw} - i_3 R_{diode} - L_f \frac{di_f}{dt} - i_f R_f \tag{13}$$

Assuming the designs of two rotating windings are identical (i.e. R_2=R_3, L_2=L_3, and M_{12}=M_{13}), replace (5), (10) and (13) into (11) and (12), i_f in the commutation phase $t\in[T_{sw}/2-\Delta t, T_{sw}/2)$ is derived by subtracting (12) from (11) as follows

$$(L_2 - M_{23} + 2L_f)\frac{di_f}{dt} + (R_{diode} + 2R_f + R_2)i_f + 2v_{fw} = 0 . \tag{14}$$

It yields

$$i_f(t) = \frac{-2v_{fw}}{R_{diode} + 2R_f + R_2} + C_2 e^{\frac{-(R_{diode}+2R_f+R_2)}{L_2 - M_{23} + 2L_f}(t - T_{sw}/2 + \Delta t)} . \tag{15}$$

When t=$T_{sw}/2$-Δt, i_f=I_{fmax}, then C_2 can be derived as

$$C_2 = \frac{(R_2 + R_{diode} + 2R_f)I_{fmax} + 2v_{fw}}{R_2 + R_{diode} + 2R_f} \tag{16}$$

Additionally, the current in field winding cannot change instantaneously, which indicates

$$\lim_{\Delta\to 0} i_f(0+\Delta) = \lim_{\Delta\to 0} i_f(\frac{T_{sw}}{2} - \Delta) = I_{fmin} \tag{17}$$

$$\lim_{\Delta\to 0} i_f(T_{sw}/2 - \Delta t - \Delta) = \lim_{\Delta\to 0} i_f(T_{sw}/2 - \Delta t + \Delta) = I_{fmax} . \tag{18}$$

Besides, assuming that the time constant of field winding is much higher than the switching period, the average field winding current I_f can be expressed as

$$I_f = \frac{2}{T_{sw}} \int_0^{\frac{T_{sw}}{2}} i_f dt \approx \frac{I_{fmax} + I_{fmin}}{2} . \tag{19}$$

By solving equations (17)-(19), the field current i_f and commutation time Δt can be obtained.

C. Linear Approximation

To simplify the analysis of the brushless exciter, it is assumed that the field current varies linearly during each operating phase. Based on the previously derived expressions from (6) and (14), assuming that the ripple in i_f is small, the rate of change of i_f during the charging and commutation phases can be approximated using average field current I_f

$$\frac{di_f}{dt} \approx \frac{\frac{M_{12}}{L_1}V_{dc} - v_{fw} - (R_2 + R_{diode} + R_f)I_f}{L_f + L_2 - \frac{M_{12}^2}{L_1}}, \quad [0, \frac{T_{sw}}{2} - \Delta t) \tag{20}$$

$$\frac{di_f}{dt} \approx \frac{-(R_{diode} + 2R_f + R_2)I_f - 2v_{fw}}{(L_2 - M_{23} + 2L_f)}, \quad [\frac{T_{sw}}{2} - \Delta t, \frac{T_{sw}}{2}) . \tag{21}$$

In steady-state operation, the net change in i_f over half a switching period T_{sw} is zero. Thus, the following equation is valid

$$\frac{\frac{M_{12}}{L_1}V_{dc} - v_{fw} - (R_2 + R_{diode} + R_f)I_f}{L_f + L_2 - \frac{M_{12}^2}{L_1}}(\frac{T_{sw}}{2} - \Delta t) + \frac{-(R_{diode} + 2R_f + R_2)I_f - 2v_{fw}}{(L_2 - M_{23} + 2L_f)}\Delta t = 0 . \tag{22}$$

Therefore, the average field current can be derived as

$$I_f = \frac{(\frac{M_{12}}{L_1}V_{dc} - v_{fw})(\frac{T_{sw}}{2} - \Delta t) - 2A_1 v_{fw}\Delta t}{A_1(R_{diode} + 2R_f + R_2)\Delta t + (R_2 + R_{diode} + R_f)(\frac{T_{sw}}{2} - \Delta t)} \tag{23}$$

where A_1 is a coefficient shown as follows:

$$A_1 = \frac{L_f + L_2 - \frac{M_{12}^2}{L_1}}{L_2 - M_{23} + 2L_f} . \tag{24}$$

In (23), the commutation time Δt represents the interval during which the current transitions from one branch to the other—specifically, from I_{fmax} to zero. Assuming the rate of change of i_f is much slower than that of the branch current, and $I_{fmax} \approx I_f$, the commutation time can be estimated from (9)-(13) as

$$\Delta t \approx \frac{(L_2 + M_{23} - 2\frac{M_{12}^2}{L_1})I_f}{\frac{M_{12}}{L_1}V_{dc} - (R_f + R_2/2 + R_{diode}/2)I_f - v_{fw}} . \tag{25}$$

It can be seen from (25) that commutation time is influenced by the magnetic coupling between the windings, which in turn depends on the air gap between the primary and secondary sides of the transformer. Under ideal condition, when there is no leakage flux in the brushless exciter (i.e. L_2=M_{23}, M_{12}^2/L_1= L_2). Then we have

$$L_2 + M_{23} - 2\frac{M_{12}^2}{L_1} = 0 . \tag{26}$$

According to (25) and (26), $\Delta t\approx 0$ can be achieved when there is a perfect coupling between primary and secondary windings. In this case, the exciter achieves its ideal output current with minimal ripple

$$I_{f\text{-}ideal} = \frac{(\frac{M_{12}}{L_1}V_{dc} - v_{fw})}{(R_2 + R_{diode} + R_f)} . \tag{27}$$

To keep the operation of SC motor, the excitation system should be designed to output high DC current and low output ripple[28]. However, in practical scenarios with larger air gaps, the mutual inductance decreases, leading to longer commutation times. This results in reduced field winding current and increased output ripple.

D. Losses Modeling

Under ideal operating conditions, SC field windings carry large currents with negligible energy dissipation. In practical systems, the electrical power required for field excitation is primarily associated with ohmic losses in the current leads and terminals rather than energy consumption within the superconducting windings. As a result, system efficiency is not a primary performance metric for the excitation system in this study. Instead, the analysis focuses on loss mechanisms in the non-superconducting components of the brushless exciter.

1). Copper Losses

Copper losses occur due to the ohmic resistance in the windings when current flows through them. These include losses in both the primary winding P_{Cu1} and the secondary windings P_{Cu2}. The total loss P_{Cu} is therefore given by

$$P_{Cu} = P_{Cu1} + P_{Cu2} = I_{1rms}^2 R_1 + \frac{1}{T_{sw}}\int_0^{T_{sw}} 2i_2^2 R_2 dt \tag{28}$$

where I_{1rms} is the root mean square (RMS) value of the primary current i_1. At high operating frequencies, additional effects such as fringing and eddy currents significantly increase the AC resistance of windings. This issue is particularly pronounced on

the secondary side of the transformer, where low voltage and high current operation are required. As a result, a moderate increase in AC resistance can lead to considerable copper losses in the secondary windings when large currents are delivered [29], [30]. Therefore, special care should be taken in the design of the secondary windings, and minimizing their AC resistance is critical for limiting copper losses in the brushless exciters.

2). Losses in Power Electronic Components

Due to the inductive nature of the load, the Si and SiC based MOSFETs in the inverter operate under soft-switching conditions. The energy stored in the inductors is sufficient to charge and discharge the drain-to-source capacitance C_{ds} during the blanking time, allowing switching losses to be neglected in this study[31]. The conduction loss in the MOSFETs is calculated based on their on-state resistance and the RMS current

$$P_{MOS} = 2I_{1rms}^2 R_{on} . \tag{29}$$

Similarly, the Schottky diodes used in the full-wave rectifier exhibit fast turn-off and zero reverse recovery characteristics, allowing their switching losses to be ignored. Only conduction losses are considered for the rectifier. The conduction loss of the rectifier is calculated as

$$\begin{aligned} P_{diode} &= v_{fw}(|i_2|+|i_3|)+\frac{1}{T_{sw}}\int_0^{T_{sw}} 2i_2^2 R_{diode}dt \\ &= v_{fw}i_f+\frac{1}{T_{sw}}\int_0^{T_{sw}} 2i_2^2 R_{diode}dt \end{aligned} \tag{30}$$

As analyzed in this study, diode losses remain a significant contributor to the overall system losses, placing requirement on the cooling system.

3). Iron Losses

Since the field winding has extremely low resistance, the system operates close to a short-circuit condition. In this state, the magnetic field generated by the primary current is effectively canceled by the field from the secondary current. As a result, the net magnetic flux in the core is minimal. Therefore, iron loss is not modeled in this study.

III. Design of Rotating Transformer

As discussed in Section II, the design of the RT plays a critical role in the performance of the brushless exciter. To ensure effective operation, the center-tap transformer must be designed to achieve low AC resistance, particularly in the secondary windings. Moreover, the resistance and inductance of the two secondary windings should be closely matched to minimize current imbalance between branches. Owing to the high turns ratio of the RT, the current on the primary side is relatively small compared to that on the secondary side. As a result, Litz wire can be employed for the primary winding, for which the AC resistance is only weakly affected by the operating frequency of the exciter. Consequently, the influence of AC resistance on the primary winding is limited, and it does not constitute a dominant design concern in this application. Therefore, the analysis and design efforts in this section focus mainly on the secondary windings, where large currents and pronounced AC effects lead to significant copper losses.

When a time-varying current conducts through the conductor, the magnetic field generated by the current affects the effective conducting area of neighbor conductors, which is known as proximity effect. In addition, the time-varying magnetic field produced by the conductor induces eddy currents within the conductor itself, which opposes the current flow in the interior region. This phenomenon is referred to as the skin effect. These effects become more pronounced at higher frequencies, resulting in an increase in the AC resistance compared to the DC resistance. The distribution of magnetic field depends on the arrangement of winding and iron core. Thus, the geometry of the RT and its operating frequency should be selected carefully.

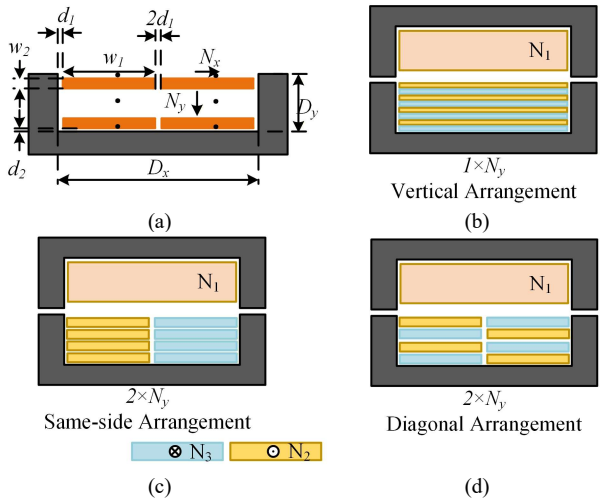

Fig. 3 Three different arrangements of secondary windings. (a) The dimensions of the secondary windings. (b) Vertical arrangements with $1\times N_y$. (c) Same-side arrangements with $N_x\times N_y$. (d) Diagonal arrangements with $N_x\times N_y$.

To identify the suitable design for the RT, three possible coil arrangements of secondary windings are considered, as illustrated in Fig. 3. The upper branch from Fig. 2, which connects to diode D_2, is labeled as winding N_2 and shown in yellow in Fig. 3 (b), (c), and (d). The lower branch, connected to diode D_3 is denoted as N_3 and shown in blue.

Denoting w_1 as the length and w_2 as the thickness of the coil, then the total number of coils in the horizontal direction N_x and in vertical direction N_y that can be filled into the window are calculated as follows

$$\begin{cases} N_x(w_1+2d_1)=D_x \\ N_y(w_2+2d_2)=D_y \end{cases} \tag{31}$$

where d_1 and d_2 are the thickness of insulation covered the coil in horizontal and vertical directions, D_x and D_y are the total length and height of the window. The three coil arrangements are described as follows:

(1) Vertical arrangement (see Fig. 3(b)): Coils are stacked vertically in a single column N_x=1. Coils are alternately assigned to N_2 and N_3 to reduce the imbalance. According to Fig. 2, N_2 conducts a full field current in phase A. During commutation phase B, the decreasing primary current i_1 reduces the magnetic field, inducing a decreasing current in N_2 and an increasing current in N_3 by the law of induction. Phases C and D follow the same principle in reverse.

(2) Same-side arrangement (see Fig. 3(c)): All coils of winding N_2 are stacked vertically on one side to reduce skin effect between

coils. However, this configuration results in a shorter total conductor length for N_2 compared to N_3, leading to imbalance.

(3) Diagonal arrangement (see Fig. 3(d)): Coils belonging to the same winding are distributed diagonally across the window. When the winding N_2 is active, coils in the diagonal position will conduct. This spatial separation reduces the proximity effect between conductors. Besides, the winding N_2 and N_3 have the same total length, improving balance.

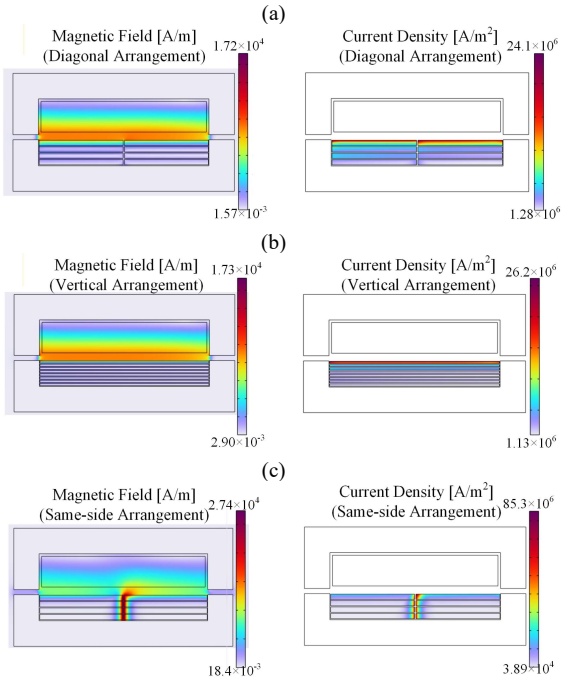

Fig. 4 Simulated magnetic field distribution (left) and current density (right) of the windings at 10kHz with (a) Diagonal arrangement (4×2). (b) Vertical arrangement (8×1). (c) Same-side arrangement (4×2).

To evaluate the AC resistance of each configuration, magnetic field and current distributions are analyzed using FEM in COMSOL Multiphysics. Without loss of generality, simulations are conducted at a winding current frequency of 10 kHz. The result is shown in Fig. 4. The value of magnetic field in the ferrite suggests that the magnetic field density in the ferrite is extremely low, resulting in neglectable iron losses in the RT. In both the vertical and diagonal arrangements, the leakage magnetic field distributes horizontally in the gap between primary and secondary sides (see Fig. 4 (a) and Fig. 4 (b)). The horizontal magnetic field causes current to concentrate on the upper surface of the coils. In same-side arrangement, however, the leakage field distributes vertically in the gap between two secondary windings. Such vertical magnetic field leads the coil current to concentrate on the shorter edge of coil (see Fig. 4 (c)). As a result, the effective conducting area of the coil decreases.

A comparison of the diagonal and same-side arrangements at 10 kHz is presented in TABLE I. The ratio between winding resistance R_2/R_3 and the ratio between mutual inductance M_{12}/M_{13} are used to describe the imbalance between windings. The ratio between average resistance and specific dc resistance $R_{ac}/R_{dc2\times1}$ is used to evaluate the increase of resistance due to the proximity effect and skin effect. Here, the DC resistance baseline is taken from the vertical 2×1 arrangement. Results show that the diagonal arrangement offers better current balance and lower average resistance compared to the same-side configuration.

TABLE I
SIMULATED WINDING RESISTANCE AND MUTUAL INDUCTANCE

Parameters (10kHz)	Diagonal (4×2)	Same-side (4×2)
Imbalance Between Winding Resistance R_2/R_3	0.924	0.582
Ratio of Mutual Inductance M_{12}/M_{13}	1	0.98
Ratio of AC Resistance $R_{ac}/R_{dc\,2\times1}$	2.99	7.45

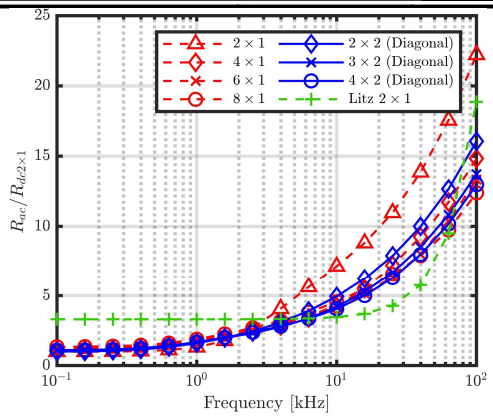

Fig. 5 The ratio between average AC resistance Rac and the specific DC resistance R_{dc} 2×1 in different arrangements. The specific DC resistance refers to the resistance with vertical 2×1 arrangement.

To further evaluate the performance of different coil arrangements, the ratio between the average AC resistance and the specific DC resistance is analyzed across a range of operating frequencies. The result is shown in Fig. 5. When the operating frequency is below 1 kHz, all winding configurations exhibit comparable AC resistance, indicating that skin and proximity effects are relatively weak in this frequency range. Under these conditions, the vertical 2×1 arrangement offers an advantage, as it represents the simplest winding topology and provides the highest copper filling factor, which is favorable from both manufacturing and cooling perspectives. However, as the operating frequency increases, the AC resistance of the vertical 2×1 configuration rises markedly compared to the other configurations. This behavior can be explained by the current distribution shown in Fig. 4 (a) and Fig. 4 (b). In the vertical arrangement, the coils located at the bottom of the trench exhibit lower current density than those positioned near the top. This uneven current distribution indicates that the effective conducting area is reduced, leading to increased AC resistance.

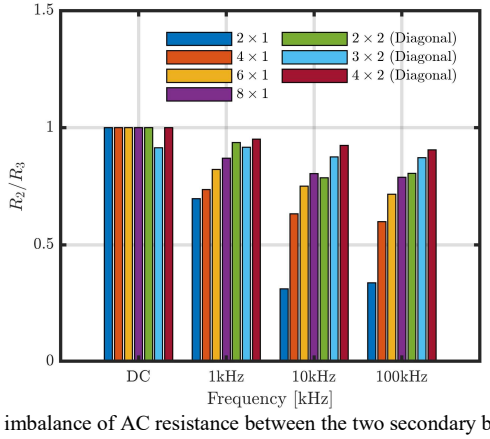

Fig. 6 The imbalance of AC resistance between the two secondary branches.

In addition to increasing AC resistance, high-frequency

operation also leads to parameter imbalance between the two secondary branches of the transformer. Fig. 6 illustrates the ratio R_2/R_3 for different winding arrangements over a frequency range from DC to 100 kHz. As the operating frequency increases, all winding arrangements show a clear reduce in resistance balance, primarily due to proximity effects that distort the current distribution in each branch. Although the vertical 2×1 configuration arrangement exhibits the lowest average AC resistance at frequencies below 1 kHz, Fig. 6 shows that a noticeable imbalance between the secondary branches already emerges at this frequency. Hence, balanced current sharing cannot be guaranteed. Therefore, the imbalance between secondary branches must be addressed, as it can lead to unequal current stress and nonuniform loss distribution in the operation of the brushless exciter.

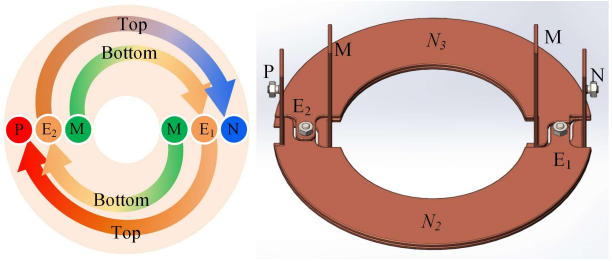

(a) (b)

Fig. 7 A schematic of the transposing winding design with vertical 2×1 arrangement.(a) Schematic. (b) Isometric view.

To mitigate the imbalance between windings, a transposed winding design is introduced. An example of the proposed transposition scheme, based on the vertical 2×1 arrangement, is shown in Fig. 7. In this configuration, the terminal P (positive) and N (negative), as illustrated in Fig. 7 (a), are connected to the rectifier diodes, while terminal M serves as the common connection point of the two secondary branches. The transposition is implemented through two exchange points, denoted as E_1 and E_2. As shown in Fig. 7 (b) when current flows through winding N_2, it travels from terminal M, passes through E_1, and exits at terminal P. Conversely, when current flows through winding N_3, it goes from M through E_2 and exits at terminal N. At the exchange points E_1 and E_2, the conductor positions are transposed between the upper and lower layers. Consequently, during each half-cycle of operation, the current path alternates between the upper and lower layers, ensuring that both winding branches experience similar magnetic field environment. By equalizing the electromagnetic environment of the two secondary windings, the transposed design effectively reduces differences between branches. As a result, the electrical symmetry of the rotating transformer is improved, leading to more balanced current sharing.

IV. Prototype Verification and System Analysis

A. Design of Prototype

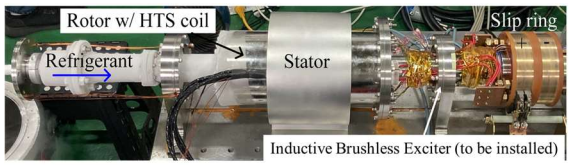

Fig. 8 Prototype of the superconducting motor

The SC motor is manufactured as shown in Fig. 8. Before the installation of the brushless exciter, the SC motor system consists of a cooling unit on the left, a stator and SC rotor in the center, and the slip rings and brushes for power supply to the HTS coils on the right. The superconducting rotor winding is modeled as a series RL branch with equivalent load resistance of R_f =1.3mΩ and equivalent load inductance of L_f=10μH. The operating current is set to 278A [32].

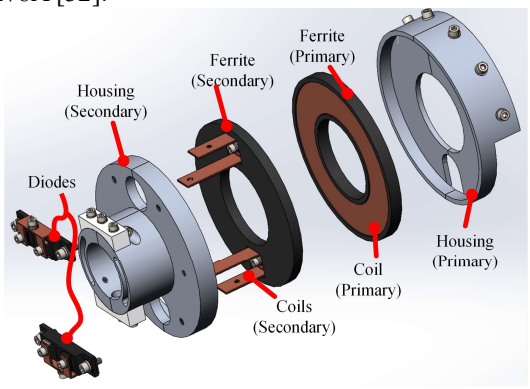

Fig. 9 Prototype of the brushless excitation system

Considering the space limitations, mechanical simplicity, and comparable electrical performance, the vertical 2×1 arrangement with winding transposition is therefore adopted for the prototype shown in Fig. 9. This choice is mainly driven by practical installation constraints. The available space to install the brushless exciter is limited, and the existing SC machine cannot be disassembled or modified. Under these conditions, the arrangement operated at 1 kHz provides the most compact and mechanically simple solution, enabling direct shaft mounting within the available space. Moreover, as shown in Section III, alternative winding arrangements do not offer a significant reduction in AC resistance or branch imbalance at the selected operating frequency.

The key dimensions of the RT are shown in Fig. 10. An isometric view of the RT is presented in Fig. 10 (a), where the transposition points and the winding outlets connected to the rectifier are highlighted. Two rectangular openings in the core serve as outlets for the secondary windings. For ease of manufacturing, the primary and secondary cores share identical outer dimensions, as illustrated in Fig. 10 (b). The rectangular windows on the secondary core are replaced by cable holes on the primary core, as shown in Fig. 10 (c).

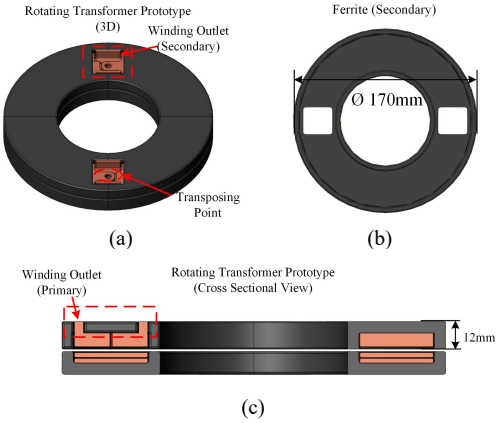

Fig. 10 Structure of the rotating transformer. (a) Isometric view of the rotating transformer. (b) Top view of the ferrite on the secondary side. (c) Cross sectional view of the rotating transformer.

To boost the output current on the secondary side, the turn ratio of the rotating transformer is set to 100:1:1 between the primary and the two secondary windings. With this high turns ratio, the primary winding carries only a relatively small AC current. The primary winding consists of 100 turns of Litz wire composed of 60 strands, each with a diameter of 0.15 mm. The thickness of the copper plate on the secondary winding is 2mm.

The key parameters of the prototype are summarized in TABLE II. In the table, the coupling factor k_{ij} between the winding i and j is defined as:

$$k_{ij} = \frac{M_{ij}}{\sqrt{L_i L_j}} \tag{32}$$

The selection of diodes for the rectifier is mainly driven by the requirement for a low forward voltage drop, which is critical for reducing conduction losses under high current operation.

TABLE II
THE KEY PARAMETERS OF THE PROTOTYPE

BES Parameters	Value
Inverter MOSFET	IPDD60R045CFD7
Rectifier Diodes	VS-440CNQ030PbF
Ferrite Core Material	PC40
Working Frequency f_{sw} (kHz)	1
Stationary Coil Resistance R_1 (mΩ)	630
Rotating Coil Resistance R_2 (mΩ)	0.11
Coupling Factors [k_{12}, k_{13}, k_{23}]	[0.98, 0.97, 0.99]
Self Inductance [L_1, L_2, L_3] (μH)	[17742, 1.74, 1.77]
Nominal Length of Airgap g (mm)	1

B. Model Verification Toward Objective Output Current

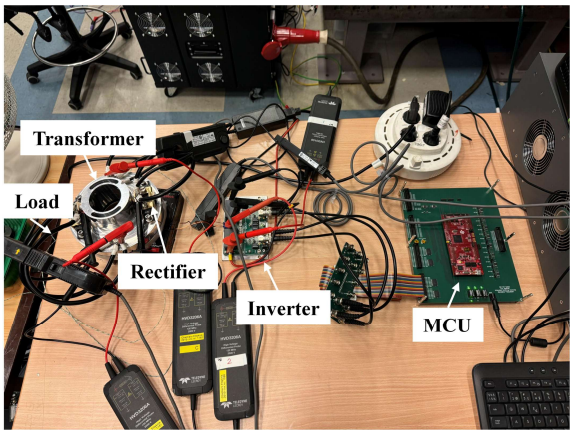

Fig. 11 Experiment setup to verify the current delivery capability of the brushless exciter.

Before assembling the BES on the shaft of SC machine, the short-circuit experiment is conducted to verify its current delivery capability. In this experiment, the BES is connected to external cables with specified electrical parameters, allowing evaluation without assembling the exciter onto the shaft of SC machine. The experimental setup is shown in Fig. 11.

The procedure of experiment and measurement setup are described as follows. The 1 kHz switching signals for the inverter are generated using a digital signal processor TMS320F28379D. The waveforms of the input voltage u_1, stationary side current i_1, load voltage u_2 and u_3, and load current i_2 and i_3 are captured using a digital oscilloscope with a bandwidth of 500 MHz. The secondary currents are measured using a current probe rated for a maximum current of 500A, while voltages are measured with differential voltage probes. The propagation delay difference among probes is compensated using DSC025 Calibration Source. The DC link voltage V_{dc} is increased gradually until the average output current reaches the target current required by the SC motor (i.e. I_f =278A). The DC link voltage is supplied by a DC power supply with a maximum output voltage 300V and a maximum output current 30A.

The BES is connected to cables with a resistance of R_f=1.3 mΩ and an inductance of L_f =0.12μH. The resistance of the cables matches that of the SC motor field winding, while the inductance is significantly lower. Nevertheless, the analytical model developed in the previous section does not assume a current-stiff load. Therefore, the validity of the model is preserved regardless of the magnitude of the load inductance.

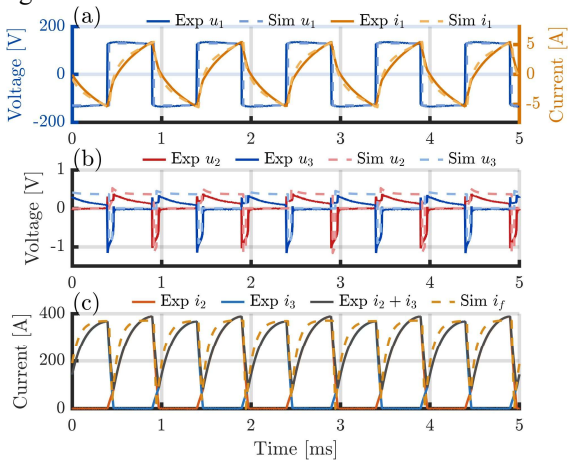

Fig. 12 Voltage and current waveforms with 1mm airgap and R_f=1.3 mΩ, L_f =0.12μH @130V V_{dc}. (a) Primary voltage and current. (b) Secondary voltage measured from the output terminals of the RT. (c) Current measured from the load.

The waveforms obtained from simulation are compared with the experimental result in Fig. 12. In the figure, the abbreviation "Sim" refers to simulation results, while "Exp" denotes experimental data. The average load current reaches 284A at V_{dc} =130V and I_{dc}=2A, while RMS value of primary AC current is 3.4A. To facilitate comparison, a phase shift is added on the experiment waveform so that the primary voltage u_1 is aligned in phase with the voltage from the simulation.

As shown in Fig. 12 (a), the zero crossing of the primary current slightly lags the switching actions, and the measured voltage waveforms are free of noticeable ringing. These results indicate soft-switching operation of the inverter. A small imbalance between the secondary branch voltages can be observed in the experimental waveforms in Fig. 12 (b). Compared with u_3, u_2 has a higher voltage during its charging phase and lower voltage during discharging phase. This imbalance may be attributed to several nonideal factors, including differences in the mutual inductances of the rotating transformer, variations in the forward voltage drops of the rectifier diodes, and unequal contact resistances in the connections. The corresponding load currents are shown in Fig. 12 (c), where the peak value of i_2 is observed to be higher than that of i_3. In the simulation, the diode parameters and the resistance of two

branches are identical, the imbalance is not shown in the simulated results.

C. Model Verification Toward Transformer Airgap

The mutual inductance and coupling factors of the transformer are strongly influenced by the length of the airgap. As the airgap increases, the magnetic reluctance of the mutual flux path between the primary and secondary windings increases. In contrast, the reluctance associated with leakage flux remains relatively unchanged. Consequently, the proportion of leakage flux rises, leading to a reduction in coupling factors between the windings.

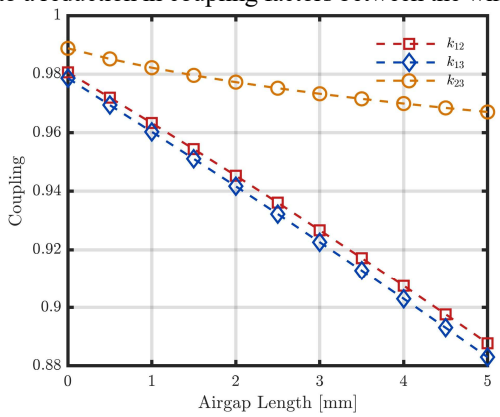

Fig. 13 The coupling factor of the transformer calculated using FEM with the length of airgap from 0mm to 5 mm.

The influence of airgap variation on the electromagnetic coupling and output current of the brushless exciter is further investigated through both simulation and experiment. As shown in Fig. 13, the coupling factors k_{12}, k_{13} and k_{23} are calculated using a FEM model for airgap lengths ranging from 0 mm to 5 mm in steps of 0.5 mm. It is observed that the difference between k_{12} and k_{13} increases as the airgap becomes larger, indicating a growing imbalance between the secondary winding.

According to equations (23) and (25), it can be inferred that lower coupling between the primary and secondary sides results in longer commutation time, which in turn leads to a reduction in output current. To validate this relationship, the output current of the brushless exciter is investigated under varying airgap conditions.

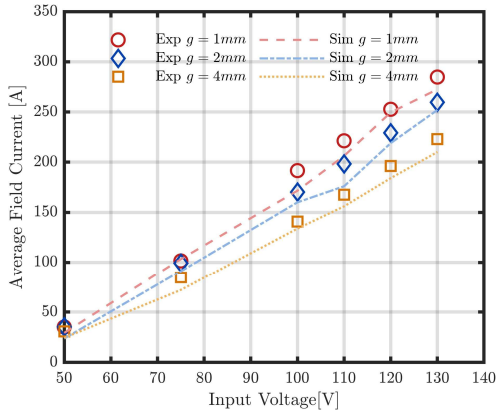

Fig. 14 The average output current with 1-, 2-, and 4-mm airgaps with R_f =1.3mΩ L_f= 0.12μH.

Fig. 14 compares the experimental and simulation results of output current for different airgap lengths. It is evident that the average output current in simulation is lower than in experiment. This can be caused by the temperature-dependent diode behavior and limitations of the diode lookup table used in the simulation. As the current increases, the diode temperature rises, causing a reduction in forward voltage drop V_{fw}. Hence, the forward voltage drop is overestimated in the simulation, resulting in lower output current. Overall, increasing the airgap from 1 mm to 4 mm results in an approximate 8.85% reduction in output current.

D. Impact of Commutation Phase

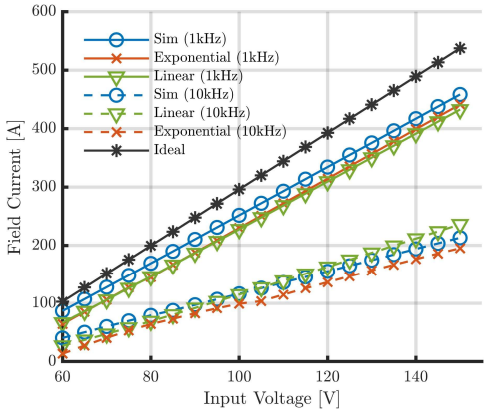

Fig. 15 Simulation result of the field current against input voltage with different operating frequency with g=1mm, R_f=1.3mΩ L_f= 10μH.

The commutation phase, which arises due to imperfect magnetic coupling, contributes to a reduction in output current. This effect becomes more pronounced at higher operating frequencies. Fig. 15 shows the relationship between the field current and input voltage for two operating frequencies: 1kHz and 10kHz. In both cases, the airgap of the rotating transformer is fixed at 1 mm, and the load is modeled as an RL branch with R_f=1.3mΩ and L_f=10uH, which represents the SC motor. The curve denoted as "Exponential" refers to the results using equations (7), (15), and (19). The curve denoted as "Linear" refers to the calculation using (23) and (25). As shown in Fig. 15, both analytical models presented in Section II align well with the simulation results when the input voltage is close to the voltage generating objective current. In the low voltage region, the error from estimation increases, this related to the discontinue current in the field. Compared with the simulation result from both the 1 kHz and 10 kHz cases, the ideal calculations from equation (27) tend to overestimate the field current, as it does not account for the commutation phase. This difference is especially evident at 10 kHz, where the commutation time occupies a larger portion of the switching period, thereby reducing the effective discharge time and resulting in a lower output current. TABLE III presents the calculated commutation time at V_{dc}=110V. When the switching frequency increases from 1kHz to 10kHz, the commutation time decreases from 41μs to 20μs. Despite the shorter duration, the relative proportion of commutation time within each switching cycle increases.

TABLE III
CALCULATION RESULT OF COMMUTATION TIME @R_f=1.3mΩ L_f=10μH

Parameters	f_{sw}=1 kHz	f_{sw}=10 kHz
DC-link Voltage V_{dc} (V)	110	
Average Field Current I_f (A)	295	140
Commutation Time Δt (μs)	41	20

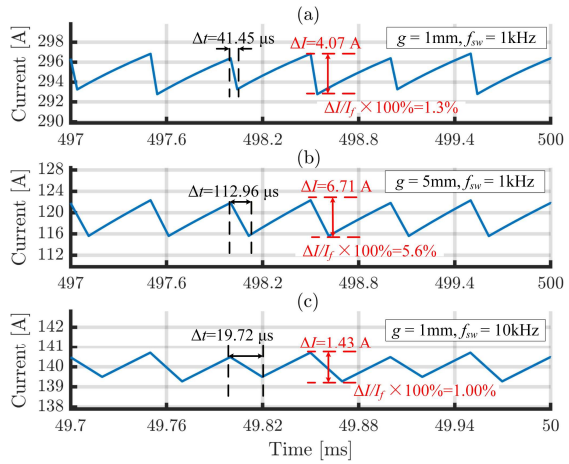

Fig. 16 Simulation result of the field current ripple and the commutation time with R_f =1.3mΩ L_f=10μH, V_{dc}=110V. (a) g=1mm, f_{sw}=1kHz. (b) g=5mm, f_{sw}=1kHz. (c) g=1mm, f_{sw}=10kHz.

The simulated field current ripple at V_{dc}= 110V with different airgap lengths and operating frequency is shown in Fig. 16. In the nominal design with airgap length g =1mm and operating frequency f_{sw} =1kHz, the magnitude of the AC ripple is 1.3% of the DC component (Fig. 16 (a)). The magnitude and the percentage of current ripple increase when the airgap length increases to 5mm (Fig. 16 (b)), which impose additional thermal load on the superconductor. To mitigate the current ripple, a higher operating frequency can be selected. As it is shown in Fig. 16 (c) that the current ripple reduced to less than 1% when the system works in 10kHz.

E. Losses Analysis

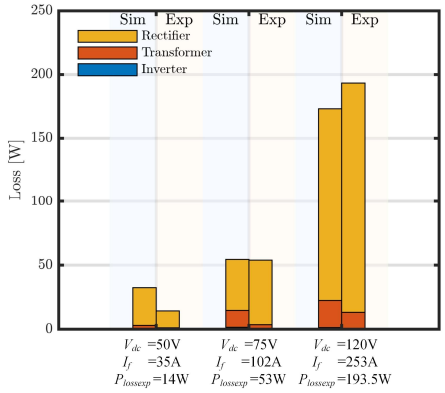

Fig. 17 Losses in each component of the brushless exciter with R_f =1.3mΩ L_f= 0.12μH.

Fig. 17 shows the loss distribution across different components of the BES. The column denoted as "Exp" is calculated from the experiment waveforms. The transformer loss is calculated as the difference between the input and output of the transformer. The results show that the transformer losses account for only 10% of the total system losses when the output is near the targeting current. Due to the low conduction loss and the soft switching condition on the primary side, the inverter losses are minimal. The secondary side operates at high current levels, resulting in significant power loss in the diode rectifier. According to experiment results, the rectifier loss reaches approximately 180 W when delivering the target field current, indicating a substantial thermal load on the diodes.

Nevertheless, the thermal management of the rectifier is effectively addressed. The aluminum housing provides good thermal contact with the rectifier, ensuring low thermal resistance between the diodes and the ambient environment. In addition, the rotational motion of the SC motor during operation enhances convective air cooling, which helps alleviate thermal stress on the rectifier.

To mitigate the high losses associated with high current operation, the SC rotor can be designed with a higher number of turns and a lower field current while maintaining the same excitation flux. This approach reduces the current level and, consequently, the rectifier losses. However, such a design change leads to longer superconducting conductors with smaller cross-section. Moreover, the higher output voltage can increase iron losses and primary side losses. Therefore, minimizing the overall losses requires a global optimization involving both the SC machine design and the excitation system.

F. Test with SC Motor

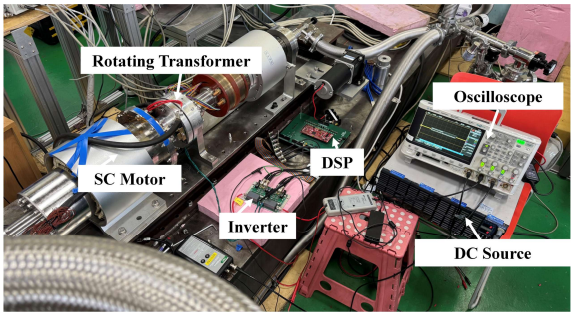

Fig. 18 Test bench with the brushless exciter mounted on the shaft of SC motor with 5mm airgap. The motor is rotating @300 RPM.

The brushless exciter is assembled and tested with the SC motor. The experiment setup is shown in Fig. 18. The rotating transformer is mounted with an airgap of 5 mm on the test bench. As discussed in the previous section, a larger airgap leads to a reduction in field current and an increase in current ripple. However, this does not compromise the validation of the electromagnetic performance of the prototype.

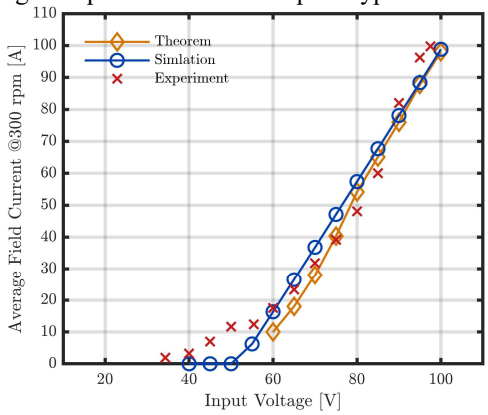

Fig. 19 The field current against input voltage with 5mm airgap. In the experiment, the field current is measured at 300RPM shaft speed. Simulation and theorem calculation results are obtained with g=5mm, R_f =1.3mΩ L_f= 10μH.

During testing, the input voltage from the DC source is gradually increased while measuring the field coil current, with the shaft rotating at 300 revolutions per minute (RPM). The test results are presented in Fig. 19. Initially, when the input voltage is below 30 V, no field current is observed due to the forward

bias threshold of the diodes. As the input voltage increases, the diodes enter the linear conduction region, allowing current to flow. A field current of 100 A is achieved when the input voltage reaches 100 V and the input current reaches 1.3A. The theoretical calculations and simulation results show good agreement with the experimental data when the input voltage is higher than 60V. The mismatch observed at low voltage levels can be attributed to the nonlinear characteristics of the diodes, and the discontinuous conduction of the field current, which are not considered in the model. The model tends to significantly overestimate the commutation time when the diode operates in the nonlinear region. This means that the developed linear model is only valid when the diodes work in linear region.

V. Conclusion

This paper investigates the feasibility of implementing high frequency brushless exciter systems on machines with superconducting rotors. First, the operating principle of the BES was introduced, an analytical model was developed to characterize the relationships among output current, parameters, and the loss in the BES. To identify the proper winding design for the high current demanded by the SC machine, various coil arrangements in the rotating transformer were analyzed using FEM simulation. The AC resistance and imbalance of parameters between windings under different coil arrangements were investigated. Based on the analysis, a prototype system was proposed to provide power to a superconducting machine. The prototype was tested to deliver the required 287 A field winding current at an input voltage of 130 V and an input current 3.4A. The experimental results showed good agreement with the simulation and theoretical calculations. Finally, the brushless exciter was assembled on the shaft of the SC motor and tested under rotational conditions at 300 RPM. With a 5 mm airgap, the system achieved a field current of 100A at 100V, 1.3A DC input.

These results validate the feasibility and effectiveness of the proposed brushless excitation system for superconducting machines, offering a promising solution for high-current, maintenance-free field excitation. Nevertheless, several aspects require further investigation. In particular, the optimal operating frequency of the system has not been systematically determined, and the current design does not fully address loss minimization. Future work will therefore focus on developing control strategies for adaptive frequency operation, as well as optimizing system parameters to minimize losses and improve overall performance of the brushless exciter.

References

[1] R. Schiferl, A. Flory, W. C. Livoti, and S. D. Umans, “High-Temperature Superconducting Synchronous Motors: Economic Issues for Industrial Applications,” *IEEE Trans. Ind. Appl.*, vol. 44, no. 5, pp. 1376–1384, Sep. 2008, doi: 10.1109/TIA.2008.2002219.

[2] P. J. Masson and C. A. Luongo, “High power density superconducting motor for all-electric aircraft propulsion,” *IEEE Trans. Appl. Supercond.*, vol. 15, no. 2, pp. 2226–2229, Jun. 2005, doi: 10.1109/TASC.2005.849618.

[3] L. Ybanez *et al.*, “ASCEND: The first step towards cryogenic electric propulsion,” *IOP Conf. Ser. Mater. Sci. Eng.*, vol. 1241, no. 1, p. 012034, May 2022, doi: 10.1088/1757-899X/1241/1/012034.

[4] B. Gamble, G. Snitchler, and T. MacDonald, “Full Power Test of a 36.5 MW HTS Propulsion Motor,” *IEEE Trans. Appl. Supercond.*, vol. 21, no. 3, pp. 1083–1088, Jun. 2011, doi: 10.1109/TASC.2010.2093854.

[5] A. B. Abrahamsen *et al.*, “Superconducting wind turbine generators,” *Supercond. Sci. Technol.*, vol. 23, no. 3, p. 034019, Feb. 2010, doi: 10.1088/0953-2048/23/3/034019.

[6] C. Hoffmann, D. Pooke, and A. D. Caplin, “Flux Pump for HTS Magnets,” *IEEE Trans. Appl. Supercond.*, vol. 21, no. 3, pp. 1628–1631, Jun. 2011, doi: 10.1109/TASC.2010.2093115.

[7] L. J. M. van de Klundert and H. H. J. ten Kate, “Fully superconducting rectifiers and fluxpumps Part 1: Realized methods for pumping flux,” *Cryogenics*, vol. 21, no. 4, pp. 195–206, Apr. 1981, doi: 10.1016/0011-2275(81)90195-8.

[8] A. Ghabeli, E. Pardo, and M. Kapolka, “3D modeling of a superconducting dynamo-type flux pump,” *Sci. Rep.*, vol. 11, no. 1, p. 10296, May 2021, doi: 10.1038/s41598-021-89596-4.

[9] Z. Bai, C. Ma, C. Chen, and Y. Pang, “Study on the Excitation of a Bi-2223 Small Superconducting Coil by a Pulse-Type Magnetic Flux Pump,” *IEEE Trans. Appl. Supercond.*, vol. 27, no. 2, pp. 1–5, Mar. 2017, doi: 10.1109/TASC.2017.2655001.

[10] Z. Bai, C. Chen, Y. Wu, and Z. Zhen, “Effect of various pulse wave forms for pulse-type magnetic flux pump,” *Cryogenics*, vol. 51, no. 9, pp. 530–533, Sep. 2011, doi: 10.1016/j.cryogenics.2011.06.009.

[11] Y. Zhang *et al.*, “Compact Linear-Motor Type Flux Pumps With Different Wavelengths for High-Temperature Superconducting Magnets,” *IEEE Trans. Appl. Supercond.*, vol. 30, no. 4, pp. 1–5, Jun. 2020, doi: 10.1109/TASC.2020.2981296.

[12] H. Ye *et al.*, “Measuring the Output Voltage of a Linear-Motor Type Flux Pump With an Insulated HTS Coil,” *IEEE Trans. Appl. Supercond.*, vol. 30, no. 4, pp. 1–5, Jun. 2020, doi: 10.1109/TASC.2020.2979837.

[13] J. H. P. Rice *et al.*, “Design of a 60 kA Flux Pump for Fusion Toroidal Field Coils,” *IEEE Trans. Appl. Supercond.*, vol. 32, no. 4, pp. 1–5, Jun. 2022, doi: 10.1109/TASC.2021.3137762.

[14] J. Ma, J. Geng, J. Gawith, and T. Coombs, “High-temperature superconducting (HTS) transformer-rectifier flux pump for powering no-insulation superconducting magnet with low characteristic resistance,” *Phys. C Supercond. Its Appl.*, vol. 560, pp. 1–6, May 2019, doi: 10.1016/j.physc.2019.01.013.

[15] T. Gong and L. Quéval, “A Field-Controlled High-Temperature Superconducting Switch: Experiment and Simulation,” *IEEE Trans. Appl. Supercond.*, vol. 35, no. 5, pp. 1–5, Aug. 2025, doi: 10.1109/TASC.2025.3539269.

[16] B. Leuw, J. Geng, J. H. P. Rice, D. A. Moseley, and R. A. Badcock, “A half-wave superconducting transformer-rectifier flux pump using Jc(B) switches,” *Supercond. Sci. Technol.*, vol. 35, no. 3, p. 035009, Feb. 2022, doi: 10.1088/1361-6668/ac4f3d.

[17] I. Patel *et al.*, “MATLAB Implementation of an HTS Transformer-Rectifier Flux Pump Using HTS Dynamic Voltage Switches,” *IEEE Trans. Appl. Supercond.*, vol. 32, no. 4, pp. 1–4, Jun. 2022, doi: 10.1109/TASC.2021.3131135.

[18] J. de Santiago *et al.*, “Electrical Motor Drivelines in Commercial All-Electric Vehicles: A Review,” *IEEE Trans. Veh. Technol.*, vol. 61, no. 2, pp. 475–484, Feb. 2012, doi: 10.1109/TVT.2011.2177873.

[19] M. Maier, N. Parspour, P. Kleemann, and M. Hagl, “Construction and measurements of an electrical excited synchronous machine with inductive contactless energy transfer to the rotor,” in *2017 Brazilian Power Electronics Conference (COBEP)*, Nov. 2017, pp. 1–6. doi: 10.1109/COBEP.2017.8257273.

[20] A. Griffo, R. Wrobel, P. H. Mellor, and J. M. Yon, “Design and Characterization of a Three-Phase Brushless Exciter for Aircraft Starter/Generator,” *IEEE Trans. Ind. Appl.*, vol. 49, no. 5, pp. 2106–2115, Sep. 2013, doi: 10.1109/TIA.2013.2269036.

[21] Y. Liu, D. Pehrman, O. Lykartsis, J. Tang, and T. Liu, “High frequency exciter of electrically excited synchronous motors for vehicle applications,” in *2016 XXII International Conference on Electrical Machines (ICEM)*, Sep. 2016, pp. 378–383. doi: 10.1109/ICELMACH.2016.7732554.

[22] E. M. Illiano, “Design of a highly efficient brushless current excited synchronous motor for automotive purposes,” ETH Zurich, 2014. Accessed: Sep. 01, 2025. [Online]. Available: https://www.research-collection.ethz.ch/entities/publication/9a2eeb3c-723b-4a80-a511-b5fc0c72e448

[23] J. Veitengruber, F. Rinderknecht, and H. E. Friedrich, “Design of a brushless excitation system utilizing pot cores,” *COMPEL - Int. J.*

Comput. Math. Electr. Electron. Eng., vol. 34, no. 6, pp. 1740–1757, Nov. 2015, doi: 10.1108/COMPEL-11-2014-0322.

[24] J. Li, "Brushless Excitation System," in *Design and Application of Modern Synchronous Generator Excitation Systems*, IEEE, 2019, pp. 215–254. doi: 10.1002/9781118841006.ch8.

[25] H. Chen, J. Tang, Y. Liu, B. Jiang, and L. Boscaglia, "Electromagnetic Performance Investigation of a Brushless Electrically Excited Synchronous Machine for Long-Distance Heavy-Duty Electric Vehicles," *IEEE Trans. Transp. Electrification*, vol. 11, no. 1, pp. 225–235, Feb. 2025, doi: 10.1109/TTE.2024.3388430.

[26] J. Tang, Y. Liu, and N. Sharma, "Modeling and Experimental Verification of High-Frequency Inductive Brushless Exciter for Electrically Excited Synchronous Machines," *IEEE Trans. Ind. Appl.*, vol. 55, no. 5, pp. 4613–4623, Sep. 2019, doi: 10.1109/TIA.2019.2921259.

[27] H. Krupp and A. Mertens, "Rotary Transformer Design for Brushless Electrically Excited Synchronous Machines," in *2015 IEEE Vehicle Power and Propulsion Conference (VPPC)*, Oct. 2015, pp. 1–6. doi: 10.1109/VPPC.2015.7353009.

[28] V. V. Chabanenko *et al.*, "Magnetothermal instabilities in type II superconductors: The influence of magnetic irreversibility," *J. Appl. Phys.*, vol. 88, no. 10, pp. 5875–5883, Nov. 2000, doi: 10.1063/1.1314611.

[29] P. Wang, B. N. Sanusi, T.-G. Zsurzsan, M. A. E. Andersen, and Z. Ouyang, "Three-Dimensional Interconnect LLC-DCX Converter for Datacenter Application," *IEEE Trans. Power Electron.*, vol. 40, no. 10, pp. 15306–15315, Oct. 2025, doi: 10.1109/TPEL.2025.3574041.

[30] W. G. Hurley, E. Gath, and J. G. Breslin, "Optimizing the AC resistance of multilayer transformer windings with arbitrary current waveforms," *IEEE Trans. Power Electron.*, vol. 15, no. 2, pp. 369–376, Mar. 2000, doi: 10.1109/63.838110.

[31] L. Lai, J. Huang, J. Tang, Z. Ouyang, Y. Liu, and M. A. E. Andersen, "Digital Control Implementation for Coupling Independent IPT Systems without Communication," in *2024 IEEE 10th International Power Electronics and Motion Control Conference (IPEMC2024-ECCE Asia)*, May 2024, pp. 3350–3356. doi: 10.1109/IPEMC-ECCEAsia60879.2024.10567845.

[32] H. Jang, L. Lai, B. Min, and Y. Liu, "Brushless Excitation System for High Current for Superconducting Motor," in *2025 IEEE Energy Conversion Conference Congress and Exposition (ECCE)*, Oct. 2025, pp. 1–5. doi: 10.1109/ECCE58356.2025.11260179.



Linhua Lai (Student member, IEEE) received the B.Sc. degree in electrical engineering from South China University of Technology, Guangzhou, China, in 2022. In 2024, he received the M.Sc. degree in electrical engineering from Chalmers University of Technology, Gothenburg, Sweden. He is currently pursuing the PhD. Degree in electrical engineering with Chalmers University of Technology.

His areas of interest include the reliability of SiC-based power electronic in drive inverters, the design of excitation system for electric machines.



Hyungkwan Jang received the B.S. and M.S. degrees in electrical engineering, and the Ph.D. degree from Hanyang University, Seoul, South Korea, in 2010, 2012, and 2021, respectively.

From 2013 to 2017, he was with LG Electronics. He is currently a Senior Research Engineer with Hyundai Motor Company. He is a recipient of the IEEE Second Prize Paper Award of the Electric Machines Committee of the IEEE Industry Applications Society as the first author (2026).

His research interests include design and analysis of motor/generator including superconducting motor, which are applied in mechanical and electrical systems in EV/HEV, air mobility, railway cars, automotive parts, and home appliance.

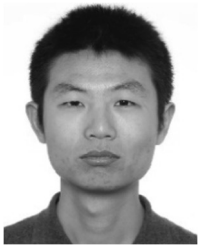

Junfei Tang (Member, IEEE) Junfei Tang received the B.Eng. degree in electrical engineering from Jiangsu University, Zhenjiang, China, in 2013, and the M.Sc. and Ph.D. degrees in electric power engineering from Chalmers University of Technology, Gothenburg, Sweden, in 2016 and 2021, respectively.

He is now working on motor drive systems in Volvo Technology.



Byungho Min received the B.S. and M.S. degrees in metal material engineering from Yonsei University, Seoul, South Korea, in 2008 and 2010, respectively.

From 2010, he has been a Senior Research Engineer with Hyundai Motor Company.

His research interests include cryogenic and structural materials which are applied in mechanical, and electrical systems in EV/HEV and air mobility.



Yujing Liu (Senior Member, IEEE) received the B.Sc., M.Sc., and Ph.D. degrees in electrical engineering from Harbin Institute of Technology, Harbin, China, in 1982, 1985, and 1988, respectively.

From 1996 to 2013, he worked with ABB Corporate Research, Västerås, Sweden. Since 2013, he has been a Professor of electrical power engineering with the Chalmers University of Technology, Gothenburg, Sweden. His research interests include the research on motors, converters, and wireless charging for electric vehicles; generators and power electronics for tidal power conversion; and high-efficiency machines for energy saving in industrial applications.

Dr. Liu is a member of the Swedish Standard Committee on Electrical Machines.